Received: 13 February 2017 | Revised: 25 July 2017 | Accepted: 4 September 2017

DOI: 10.1002/nme.5699

RESEARCH ARTICLE

WILEY

A quasi-static discontinuous Galerkin configurational force crack propagation method for brittle materials

Robert Bird | Will Coombs | Stefano Giani

School of Engineering and Computing Sciences, Durham University, Science Site, South Road, Durham, DH1 3LE, UK

Correspondence
Robert Bird, School of Engineering and Computing Sciences, Durham University, Science Site, South Road, Durham, DH1 3LE, UK.
Email: robert.e.bird@durham.ac.uk

Funding information
Engineering and Physical Sciences Research Council, Grant/Award Number: EP/M507854/1

Summary

This paper presents a framework for r-adaptive quasi-static configurational force (CF) brittle crack propagation, cast within a discontinuous Galerkin (DG) symmetric interior penalty (SIPG) finite element scheme. Cracks are propagated in discrete steps, with a staggered algorithm, along element interfaces, which align themselves with the predicted crack propagation direction. The key novelty of the work is the exploitation of the DG face stiffness terms existing along element interfaces to propagate a crack in a mesh-independent r-adaptive quasi-static fashion, driven by the CF at the crack tip. This adds no new degrees of freedom to the data structure. Additionally, as DG methods have element-specific degrees of freedom, a geometry-driven p-adaptive algorithm is also easily included allowing for more accurate solutions of the CF on a moving crack front. Further, for nondeterminant systems, we introduce an average boundary condition that restrains rigid body motion leading to a determinant system. To the authors' knowledge, this is the first time that such a boundary condition has been described. The proposed formulation is validated against single and multiple crack problems with single- and mixed-mode cracks, demonstrating the predictive capabilities of the method.

KEYWORDS

configurational force, crack propagation, discontinuous Galerkin, rp-adaptivity

1 | INTRODUCTION

Recently, there has been significant interest in the numerical prediction of crack propagation. However, despite numerous frameworks being proposed, accurate and efficient simulation of crack probation is still one of the most challenging problems in solid mechanics. The fracture mechanics community requires algorithms that can predict the evolution of cracks from initiation through to large-scale propagation. In this paper, we present an algorithm based on the concept of configurational forces (CFs) combined with a discontinuous Galerkin (DG) numerical framework that allows for efficient brittle crack propagation in 2 dimensions.

The work of Eshelby,[1,2] Rice,[3] and Irwin[4,5] are fundamental to all work in this field. The local variational formulations in previous studies[6-12] use a CF acting at a crack tip to describe the propagation of a crack. The CF values have been determined numerically at static fracture fronts by other studies.[13-16] Using the CF to describe a moving fracture front was initially attempted by Mueller and Maugin[17] within the conventional finite-element context and Larsson and

Fagerström[18,19] in XFEM, with an optimally convergent DG-XFEM achieved by Shen and Lew.[20] Later, a robust r-adaptive technique was defined by Miehe and coworkers[21-23] for propagating cracks, which was also taken to 3 dimensions by Kaczmarczyk et al.[24] Furthermore, the framework has recently been applied to materials with non-linear behaviour, see for example, the works of Runesson et al[25] and Tillberg and Larsson[26] on elasto-plasticity and Näser et al[27,28] on time-dependent materials and the review by Özenç et al.[29]

An alternative to CF crack propagation is the path independent J-integral.[3] Ishikawa et al[30] demonstrated that the J-integral is the sum of its mode 1 and mode 2 counterparts, from which the respective stress intensity factors (SIFs) can be found. The SIFs are evaluated separately by decomposing the stress and displacement field about the crack tip.[31] The crack direction can then be determined by the maximal principal stress criterion.[32] Mixed mode cracks can also be analysed using the "Gθ method," see Destuynder et al,[33] in conjunction with the maximum strain energy release rate criterion.[34] The Gθ can also be used in conjunction with the maximum circumferential stress criterion (MCSC)[32] or the minimum strain energy density criterion.[35] Further, the virtual crack extension method can be used to model mixed mode problems. The virtual crack extension method was introduced independently by deLorenzi[36] and other works.[37-41]

Hansbo and Hansbo[42,43] present a crack propagation method, for linear and non-linear elasticity, using DG methods. However, similar to Heintz,[44] the crack propagation techniques proposed in these papers do not exploit the face communication at element interfaces that exist in DG methods. This is similar to several continuous Galerkin (CG) methods where the elements are split internally. Arranz et al[45] very briefly outlined the advantages of using weak element face terms to propagate a crack; however, they do not provide any algorithm to do so.

The hybrid DG method exploits element interfaces and element specific degrees of freedom (dof) to propagate a crack using a cohesive zone; initial works include Mergheim et al[46,47] and Huang and Costanzo.[46,47] However, this method is strongly mesh-dependent as the failure criterion is defined across element interfaces rather than nodes at the crack tip. Cracks can therefore only exist at the initialised boundaries of elements of the original mesh, unlike the r-adaptive method provided by Miehe et al[21] where the element interfaces adapt and align with the predicted crack direction. Accurate solutions for crack propagation paths can only be obtained with very refined meshes.[48] Hybrid DG methods have also been explored by previous works,[48-51] amongst others. Within the context of cohesive law fracture, h- and hp-adaptive schemes, respectively,[52,53] have been produced for space-time DG methods. Additionally, a review of the cohesive laws, which drive the traction-separation is provided by Park and Paulino.[54] In this paper, we combine the mesh-independent r-adaptive CF crack propagation method provided by Miehe et al[21] with a DG formulation, to take an advantage of the element-specific dof along element interfaces to propagate a crack in a mesh independent fashion.

The DG methods were first introduced by Reed et al[55] for solving the neutron transport equation. Richter[56] prompted an extension of the original DG method to elliptical problems including linear convective-diffusion terms. However, the discontinuous approximation was only applied for the convective terms, with mixed methods for the second-order elliptic operators. Bassi and Rebay[57] introduced the complete discontinuous approximations for both the convective and second-order elliptical operators. A review of the use of DG methods for elliptical problems can be found in Arnold;[58] from here, the SIPG method can be found. In this paper, the bilinear weak form for linear hyperelastic problems proposed by Hansbo and Larson[59] is used.

After this introduction, the paper is split into 5 further sections. In Section 2, the CF method for fracture propagation is outlined, based on the work of Miehe et al,[21] Miehe and Gürses,[22] and Gürses and Miehe.[23] In Section 3, the DG finite element framework, in which the fracture propagation model is cast, is defined. This includes all weakly applied homogeneous and heterogeneous boundary conditions for linear elasticity. In Section 4, the different methods for calculating the CF are described. Section 5 contains the novel numerical implementation of the CF method within the DG framework using an rp-adaptive scheme. Specifically, we exploit the element specific dof and the weak interaction between elements, existing as stiffness terms in the global stiffness matrix, to propagate a crack. Also included in Section 5 is a description of the average boundary conditions, which are used to make a problem determinant when only tractions are applied to the boundaries. Section 6 presents numerical examples, which demonstrate the accuracy of calculating the CF, in terms of both magnitude and direction for static, quasi-static, mode 1, and mixed mode problems. Conclusions are drawn in Section 7.

2 | CONFIGURATIONAL FORCE FRACTURE

This section provides the key equations for the small strain description of the CF approach to modelling brittle fracture based on the work of Miehe et al.[21] The continuous formulation is valid for both 2D and 3D; however, the discrete formulation is different, see Gürses and Miehe[23] and Kaczmarczyk et al[24] for variations of the 3D discrete formulation within a CG framework.

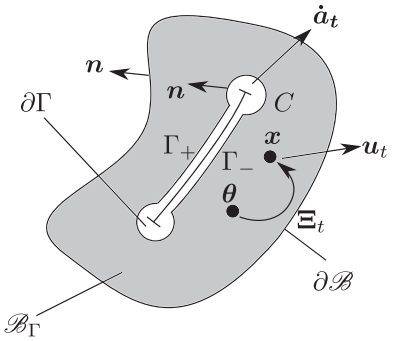

FIGURE 1 Configurational force quantities defined on the material domain $\mathscr{B}_\Gamma$ (adapted from Miehe et al[21])

2.1 | Continuous formulation in space and time

Consider the homogeneous evolving material body in Figure 1, $\mathscr{B}\subset\mathscr{R}^3$, which has an exterior boundary $\partial\mathscr{B}$, crack lips Γ, and crack tip $\partial\Gamma$. The subset $\mathscr{B}_\Gamma = \mathscr{B}\backslash\Gamma\cup\partial\Gamma$ is defined with the crack lips Γ^+ and Γ^- and the surface C encircling the crack front. In the limit $\Gamma^+\to\Gamma$, $\Gamma^-\to\Gamma$, and $C\to\partial\Gamma$. Finally $\partial\mathscr{B}_\Gamma = \partial\mathscr{B}\cup\Gamma^-\cup\Gamma^+\cup C$ is a set containing all the boundaries of the problem. Here, $\partial\mathscr{B}=\mathscr{B}_D\cup\mathscr{B}_N\cup\mathscr{B}_T$ where $\mathscr{B}_D$, $\mathscr{B}_N$, and $\mathscr{B}_T$ are the Dirichlet, Neumann, and roller boundary conditions, respectively.

The material points are defined $\boldsymbol{x}\in\mathscr{B}_\Gamma$. They evolve from a set of reference coordinates $\boldsymbol{\theta}\in\Omega$, where $\Omega\subset\mathscr{R}^3$ is the reference domain. This is achieved by using the time-dependent mapping $\boldsymbol{\Xi}_t(\boldsymbol{\theta})=\boldsymbol{x}$, which allows for a change in material structure that reflects the propagation of a crack. The small strain displacement at time $t\in\mathscr{R}^+$ is defined as

$$\boldsymbol{u}_t = \begin{cases} \mathscr{B}_\Gamma\to\mathscr{R}^3 \\ \boldsymbol{x}\to\boldsymbol{u}(\boldsymbol{x})_t. \end{cases} \tag{1}$$

Next, we define the global power postulate of the mechanical form of the second law of thermodynamics for power dissipation, $\mathscr{D}$,

$$\mathscr{D} := \mathscr{P} - \frac{\mathrm{d}}{\mathrm{d}t}\Psi \geq 0, \quad \mathscr{P} = \int_{\partial\mathscr{B}} \boldsymbol{t}\cdot\dot{\boldsymbol{u}}\mathrm{d}S \quad \text{and} \quad \Psi = \int_{\mathscr{B}_\Gamma}\hat{\psi}(\boldsymbol{\varepsilon})\mathrm{d}V. \tag{2}$$

$\mathscr{P}$ is the power applied to the boundary $\partial\mathscr{B}$ by a traction $\boldsymbol{t}$, $\hat{\psi}$ is the free energy function, and $\boldsymbol{\varepsilon}$ is the infinitesimal strain

$$\boldsymbol{\varepsilon} = \frac{1}{2}\left[(\partial\boldsymbol{u}_t/\partial\boldsymbol{x})^T + \partial\boldsymbol{u}_t/\partial\boldsymbol{x}\right]. \tag{3}$$

Following the work by Miehe et al,[21] (2_1) becomes

$$\mathscr{D} = \mathscr{P} - \int_{\mathscr{B}_\Gamma}(\boldsymbol{\sigma} : \boldsymbol{\nabla}\boldsymbol{v} + \Sigma : \boldsymbol{\nabla}\boldsymbol{V})\mathrm{d}V \geq 0, \tag{4}$$

where $\boldsymbol{\sigma} = \boldsymbol{\nabla}_\varepsilon\hat{\psi}(\boldsymbol{\varepsilon})$ is Cauchy stress, $\boldsymbol{\Sigma} = \psi(\boldsymbol{\varepsilon})\boldsymbol{\delta} - (\partial\boldsymbol{u}_t/\partial\boldsymbol{x})^T\boldsymbol{\sigma}$ is the Eshelby stress, and $\boldsymbol{\delta}$ is an identity matrix. The boundary conditions for the spacial velocity field $\boldsymbol{v}$ are

$$\boldsymbol{v}\in\{\boldsymbol{v}|\boldsymbol{v}=\bar{\boldsymbol{v}} \text{ on } \partial\mathscr{B}_D\}, \quad \text{where} \quad \boldsymbol{v} = \frac{\partial\boldsymbol{u}_t(\boldsymbol{x})}{\partial t}, \tag{5}$$

which has a prescribed value $\bar{\boldsymbol{v}}$ on a Dirichlet boundary $\partial\mathscr{B}_D$. The boundary conditions for the material velocity field, $\boldsymbol{V}$, are

$$\boldsymbol{V}\in\{\boldsymbol{V}|\boldsymbol{V}\cdot\boldsymbol{n}=0 \text{ on } \partial\mathscr{B}\cup\Gamma, \boldsymbol{V}=\dot{\boldsymbol{o}} \text{ on } \partial\Gamma\}, \quad \text{where} \quad \boldsymbol{V} = \left(\frac{\partial\boldsymbol{\Xi}(\theta)}{\partial t}\right)\circ\boldsymbol{\Xi}_t^{-1}(\boldsymbol{x}), \tag{6}$$

with a material velocity $\dot{\boldsymbol{o}}$ at the crack tip. Given that $\boldsymbol{v}$ and $\boldsymbol{V}$ are arbitrary in $\mathscr{B}_\Gamma$ and have boundary conditions (5) and (6), respectively, the following statements of equilibrium can be defined

$$\boldsymbol{\nabla}\cdot\boldsymbol{\sigma} = 0 \text{ in } \mathscr{B}_\Gamma, \quad \boldsymbol{\sigma}\cdot\boldsymbol{n} = \boldsymbol{t} \text{ on } \partial\mathscr{B}, \quad \boldsymbol{\sigma}\cdot\boldsymbol{n} = 0 \text{ on } \Gamma, \quad \text{and} \quad \boldsymbol{\nabla}\cdot\boldsymbol{\Sigma} = 0 \text{ in } \mathscr{B}_\Gamma. \tag{7}$$

2.2 | Discrete formulation in space

A discrete formulation of the power dissipation also exists. This is taken directly from (4) using isoparametric shape functions $\boldsymbol{N_I}$, which act on a node $\boldsymbol{I}$ of element K. $K \in \mathcal{T}$, where $\mathcal{T}$ is a subdivision of the polygonal domain $\mathscr{B}_\Gamma \subset \mathbb{R}^2$ into disjoint triangular elements, with its coordinates mapped into the reference domain using $\boldsymbol{\Xi}_t^{-1}(\boldsymbol{x})$. The nodal material and spacial velocities existing on element K are respectively $\dot{\boldsymbol{D}}_{\boldsymbol{I}}$ and $\dot{\boldsymbol{d}}_{\boldsymbol{I}}$. The derivative of the shape functions in the material domain $\boldsymbol{B_I}(\boldsymbol{x}) = \nabla_{\boldsymbol{x}}\boldsymbol{N_I}$ also exists. Equation 4 can be discretised into the form

$$\mathscr{D} = \sum_{\boldsymbol{I}=1}^{n_I}([\boldsymbol{f_I} + \boldsymbol{p_I}] \cdot \dot{\boldsymbol{d}}_{\boldsymbol{I}} + \boldsymbol{g_I} \cdot \dot{\boldsymbol{D}}_{\boldsymbol{I}}) \geq 0, \tag{8}$$

where $n_{\boldsymbol{I}}$ is the set of all element nodes in the mesh. The conventional force components in (8) are defined as

$$\boldsymbol{f_I} = -\mathrm{A}_{K=1}^{\mathcal{T}} \int_K \boldsymbol{B_I}^{\mathrm{T}} \boldsymbol{\sigma}^h \mathrm{d}V \quad \text{and} \quad \boldsymbol{p_I} = \mathrm{A}_{K=1}^{\mathcal{T}} \int_{\partial K} \boldsymbol{N_I}^{\mathrm{T}} \boldsymbol{t}^h \mathrm{d}V \tag{9}$$

and the CF is

$$\boldsymbol{g_I} = -\mathrm{A}_{K=1}^{\mathcal{T}} \int_K \boldsymbol{B_I}^{\mathrm{T}} \Sigma^h \mathrm{d}V. \tag{10}$$

A is the usual finite element summation operator. Additionally, the material and spacial velocities in element K take the discrete form, denoted by the superscript h,

$$\boldsymbol{V}_t^h = \boldsymbol{N_I}(\boldsymbol{x})\dot{\boldsymbol{D}}_{\boldsymbol{I}} \quad \text{and} \quad \boldsymbol{v}_t^h = \boldsymbol{N_I}(\boldsymbol{x})\dot{\boldsymbol{d}}_{\boldsymbol{I}}, \tag{11}$$

with all interpolation occurring in the material domain, where

$$\dot{\boldsymbol{d}}_{\boldsymbol{I}} \in \{\dot{\boldsymbol{d}}_{\boldsymbol{I}} | \dot{\boldsymbol{d}}_{\boldsymbol{I}} = \bar{\boldsymbol{d}}_{\boldsymbol{I}} \text{ on } \partial\mathscr{B}_D\} \tag{12}$$

is a prescribed displacement on the boundary and,

$$\dot{\boldsymbol{D}}_{\boldsymbol{I}} \in \{\dot{\boldsymbol{D}}_{\boldsymbol{I}} | \dot{\boldsymbol{D}}_{\boldsymbol{I}} \cdot \boldsymbol{n} = 0 \text{ on } \partial\mathscr{B} \cup \Gamma, \dot{\boldsymbol{D}}_{\boldsymbol{I}} = \dot{\boldsymbol{o}}_{\boldsymbol{I}} \text{ on } \partial\Gamma\}, \tag{13}$$

where $\dot{\boldsymbol{o}}_{\boldsymbol{I}}$ is the crack tip material velocity. A consequence of (12) is that the following is true

$$\boldsymbol{f_I} = 0 \text{ in } \mathscr{B}_\Gamma, \quad \boldsymbol{f_I} + \boldsymbol{p_I} = \boldsymbol{0} \text{ on } \partial\mathscr{B}, \quad \text{and} \quad \boldsymbol{f_I} = \boldsymbol{0} \text{ on } \Gamma. \tag{14}$$

This means that the reduced discretised global power dissipation (8) at the crack tip is

$$\mathscr{D}^h = \sum_{I \in \partial\Gamma} \boldsymbol{g_I} \cdot \dot{\boldsymbol{o}}_{\boldsymbol{I}}. \tag{15}$$

$\boldsymbol{g_I}$ is the CF ; it determines crack growth and direction and is calculated in post processing procedure, once the linear elastic system has been solved.

2.3 | Discrete formulation in time

The final step is determining how the crack will propagate. Here, we will use a quasi-static crack propagation framework as presented in Miehe et al,[21] Miehe and Gürses[22] to perform a quasi static analysis. First, we integrate the discrete dissipation power at the crack, (15), over the time period $[t^n, t^{n+1}]$

$$\Delta\mathscr{D}^h = \int_{t^n}^{t^{n+1}} \mathscr{D}^h \mathrm{d}t \approx \sum_{I \in \partial\Gamma} \boldsymbol{g_I} \cdot \Delta\boldsymbol{o_I}. \tag{16}$$

This gives an incremental constant increase in the crack surface length, $\Delta\boldsymbol{o_I}$, over the time period $[t^n, t^{n+1}]$. It has the form

$$\Delta\boldsymbol{o_I} = \Delta\gamma_I \frac{\boldsymbol{g_I}}{|\boldsymbol{g_I}|}, \quad \text{where} \quad \Delta\gamma_I = \begin{cases} h_o \text{ for } |\boldsymbol{g_I}| \geq g_c \\ 0 \quad \text{otherwise,} \end{cases} \tag{17}$$

where g_c is a Griffith material failure criteria. h_o is the increase in crack length defined as $h_o = \boldsymbol{g_I}/|\boldsymbol{g_I}| \cdot L_c$, L_c is the original length of the most aligned element face with $\boldsymbol{g_I}/|\boldsymbol{g_I}|$. A crack will propagate the entire reorientated element face associated with L_c. $\Delta\gamma_I$ is subject to the Karush-Kuhn-Tucker conditions

$$\Delta\gamma_I \geqslant 0, \quad (|\boldsymbol{g_I}| - g_c) \leqslant 0 \quad \text{and} \quad \Delta\gamma_I(|\boldsymbol{g_I}| - g_c) = 0. \tag{18}$$

Motion of nodes can be permitted in the material configuration, except motion that would change the shape of the boundary. We recognise that is possible to dissipate power by moving nodes in the material configuration[60,61] and thus achieve a minimal energy solution to the problem by increasing the total power dissipated by the term $\sum_{I=1}^{n_I} \boldsymbol{g_I} \cdot \dot{\boldsymbol{D}}_{\boldsymbol{I}}$ in (8). However this is a highly non-linear problem and therefore computationally expensive. We therefore do not solve for it here, consistent with the works of previous studies[16,21-23,42,43,45] and many others but instead recognise that it could potentially improve our solutions. Here, we only consider power dissipation in the form of surface generation, or crack propagation, when the Griffith failure criterion $|\boldsymbol{g_I}| > g_c$ is satisfied at a crack tip.

The key equations for modelling brittle fracture propagation based on CF have now been outlined. Their values are calculated in a post-processing procedure once the linear elastic system for small strain problems has been solved. The linear elastic system is cast within a DG framework presented in the next section. It should also be stated that it is possible to simultaneously solve for the CF and material velocity as in Kaczmarczyk et al,[24] based on the works of Kuhl et al.[62] However, there is debate in the literature on the validity of linearising the CF in these approaches.[63]

3 | DISCONTINUOUS GALERKIN FINITE ELEMENT APPROXIMATION

We consider the following model problem on a bounded Lipschitz polygonal material domain $\mathscr{B}_\Gamma$ in $\mathbb{R}^2$, with $\partial\mathscr{B}_N \cup \partial\mathscr{B}_D \cup \partial\mathscr{B}_T = \partial\mathscr{B}_\Gamma$. In this section, three different boundary conditions are described within the DG formulation. On $\partial\mathscr{B}_D$, Dirichlet boundary conditions are applied; the prescribed displacement on this boundary has a value $\boldsymbol{g}_D$. On $\partial\mathscr{B}_N$, Neumann boundary conditions are applied; here, the traction has a value $\boldsymbol{g}_N$. Last, a roller boundary condition is applied on $\partial\mathscr{B}_T$; here, the tangential component to the boundary surface has a value of zero, and the displacement normal to the surface has the value $\boldsymbol{g}_T \cdot \boldsymbol{n}$, where $\boldsymbol{n}$ is the unit vector normal to the boundary. The strong form of the problem with the boundary conditions is defined as

$$\begin{aligned} &\boldsymbol{\nabla}\cdot\boldsymbol{\sigma}(\boldsymbol{u}) = 0 \text{ in } \mathscr{B}_\Gamma, \quad \boldsymbol{\sigma}(\boldsymbol{u})\cdot\boldsymbol{n} = \boldsymbol{g}_N \text{ on } \partial\mathscr{B}_N, \\ &\boldsymbol{u} = \boldsymbol{g}_D \text{ on } \partial\mathscr{B}_D, \quad (\boldsymbol{\sigma}(\boldsymbol{u})\boldsymbol{n})\cdot\boldsymbol{n}^{\parallel} = \boldsymbol{0} \text{ on } \partial\mathscr{B}_T, \quad \text{and} \quad \boldsymbol{u}\cdot\boldsymbol{n} = \boldsymbol{g}_T\cdot\boldsymbol{n} \text{ on } \partial\mathscr{B}_T, \end{aligned} \tag{19}$$

where $\boldsymbol{n}^{\parallel}$ is the tangential unit vector to the boundary. The prescribed values on the respective boundaries, $\boldsymbol{g}_D$, $\boldsymbol{g}_T$, and $\boldsymbol{g}_N$, are the prescribed displacements (fully prescribed $\boldsymbol{g}_D$ and roller $\boldsymbol{g}_T$) and the traction vector $\boldsymbol{g}_N$.

Each element K of the mesh $\mathcal{T}$, where $\mathcal{T}$ is in general irregular, is the image of the reference triangle under an affine elemental mapping $F_K : \hat{K} \to K$. We denote by $\mathcal{F}(K)$ the set of the 3 elemental faces of an element K. If the intersection $F = \partial K \cap \partial K'$ of 2 elements $K, K' \in \mathcal{T}$ is a segment, we call F an interior face of $\mathcal{T}$. The set of all interior faces is denoted by $\mathcal{F}_I(\mathcal{T})$. Analogously, if the intersection $F = \partial K \cap \partial\mathscr{B}_\Gamma$ of an element $K \in \mathcal{T}$ and $\partial\mathscr{B}_\Gamma$ is a segment, we call F a boundary face of $\mathcal{T}$. The set of all boundary faces of $\mathcal{T}$ is denoted by $\mathcal{F}_B(\mathcal{T})$, and it is the union of the 3 sets $\mathcal{F}_N(\mathcal{T})$, $\mathcal{F}_D(\mathcal{T})$, and $\mathcal{F}_T(\mathcal{T})$ of faces on the 3 boundaries $\partial\mathscr{B}_N$, $\partial\mathscr{B}_D$, and $\partial\mathscr{B}_T$, respectively. Additionally the internal crack is represented by tractions on $\partial K \cap \partial\mathscr{B}_N \cap (\Gamma^+ \cup \Gamma^-)$ as zero and the crack tip being represented by an element node existing at $\partial\Gamma$. Moreover, we set $\mathcal{F}(\mathcal{T}) = \mathcal{F}_I(\mathcal{T}) \cup \mathcal{F}_B(\mathcal{T})$. For each element $K \in \mathcal{T}$, we define p_K to be the order of the element. We also define the vector function $\underline{p} = \{\ p_K \ : \ K \in \mathcal{T}\ \}$.

For any mesh $\mathcal{T}$ of $\mathscr{B}_\Gamma$ with the degree vector p, we then define the hp-version DG finite element space by

$$W_{\underline{p}}(\mathcal{T}) = \{\ \boldsymbol{w} \in [L^2(\mathscr{B}_\Gamma)]^2 \ : \ \boldsymbol{w}|_K \in [\mathcal{P}_{p_K}(K)]^2, \quad K \in \mathcal{T}\ \},$$

$[L^2(\mathscr{B}_\Gamma)]^2 = [L^2(\mathscr{B}_\Gamma)] \times [L^2(\mathscr{B}_\Gamma)]$ represents the functional space of the 2 components of the function $\boldsymbol{w}$ and $\mathcal{P}_{p_K}(K)$ denotes the set of all polynomials on the triangle K of degree no more than p_K. The basis functions chosen are hierarchical,[64] with the test function and displacement described respectively as $\boldsymbol{w} = \boldsymbol{N}_s\boldsymbol{w}_s$ and $\boldsymbol{u}_h = \boldsymbol{N}\boldsymbol{u}_s$. $\boldsymbol{w}_s$, and $\boldsymbol{u}_s$ are the hierarchical basis function coefficients, and $\boldsymbol{N}_s$ are the hierarchical functions in the reference element $\hat{K}$.

We now introduce the SIPG method in the bilinear form, for the approximation of the model problem (19): Find $\boldsymbol{u}_h \in W_{\underline{p}}(\mathcal{T})$, such that

$$\boldsymbol{a}(\boldsymbol{u}_h, \boldsymbol{w}) = \boldsymbol{l}(\boldsymbol{w}), \tag{20}$$

for all $\boldsymbol{w} \in W_{\underline{p}}(\mathcal{T})$, where

$$\begin{aligned} \boldsymbol{a}_K(\boldsymbol{u}_h, \boldsymbol{w}) = &\sum_{K\in\mathcal{T}} (\boldsymbol{\sigma}(\boldsymbol{u}_h), \boldsymbol{\epsilon}(\boldsymbol{w}))_K - \sum_{F\in\mathcal{F}_I(\mathcal{T})\cup\mathcal{F}_D(\mathcal{T})} \langle\{\boldsymbol{\sigma}(\boldsymbol{u}_h)\}, [[\boldsymbol{w}]]\rangle_F \\ &- \sum_{F\in\mathcal{F}_I(\mathcal{T})\cup\mathcal{F}_D(\mathcal{T})} \langle[[\boldsymbol{u}_h]], \{\boldsymbol{\sigma}(\boldsymbol{w})\}\rangle_F + \sum_{F\in\mathcal{F}_I(\mathcal{T})\cup\mathcal{F}_D(\mathcal{T})} \beta\langle p_F^2 h_F^{-1}[[\boldsymbol{u}_h]], [[\boldsymbol{w}]]\rangle_F \\ &- \sum_{F\in\mathcal{F}_T(\mathcal{T})} \langle(\boldsymbol{u}_h\cdot\boldsymbol{n})\boldsymbol{n}, \boldsymbol{\sigma}(\boldsymbol{w})\boldsymbol{n}\rangle_F - \sum_{F\in\mathcal{F}_T(\mathcal{T})} \langle\boldsymbol{\sigma}(\boldsymbol{u}_h)\boldsymbol{n}, (\boldsymbol{w}\cdot\boldsymbol{n})\boldsymbol{n}\rangle_F \\ &+ \sum_{F\in\mathcal{F}_T(\mathcal{T})} \beta p_F^2 h_F^{-1} \int_F (\boldsymbol{u}_h\cdot\boldsymbol{n})(\boldsymbol{w}\cdot\boldsymbol{n})\mathrm{d}S, \end{aligned} \tag{21}$$

where β is a penalty term for linear elastic SIPG

$$\beta = \frac{\delta E_Y \nu}{(1+\nu)(1-2\nu)}. \tag{22}$$

In this paper, $\delta = 10$, its range is defined by Hansbo and Larson,[59] E_Y the material's Young's modulus, and ν as Poisson's ratio. Further, h_F is the element face length and

$$p_F = \begin{cases} \max(p_K^+, p_K^-) & \text{if } F \in \mathcal{F}_I(\mathcal{T}) \\ p_K^+ & \text{if } F \in \mathcal{F}_B(\mathcal{T}), \end{cases} \tag{23}$$

where $\{\cdot\}$, $[[\cdot]]$, $(\cdot,\cdot)$ and $\langle\cdot,\cdot\rangle$ are defined in Arnold et al.[65]

The first term on the right hand side of (21) describes the virtual energy in the material bulk. The second is a face stiffness term, which averages the jumps in tractions existing between elements. This is followed by its transpose to make the global stiffness matrix symmetric. The fourth term is required to stabilise the method. The last 3 terms impose the conditions on the boundary $\partial\mathscr{B}_T$ weakly, the first of the 3 terms is the weak implementation of the boundary, and the next is the transpose followed again by a term to stabilise the method.

The right hand side of (20) has the form

$$\begin{aligned} \boldsymbol{l}(\boldsymbol{w}) = &- \sum_{F\in\mathcal{F}_D} \langle\boldsymbol{g}_D, \boldsymbol{n}\cdot\boldsymbol{\sigma}(\boldsymbol{w})\rangle_F + \sum_{F\in\mathcal{F}_D(\mathcal{T})} \beta\langle p_F^2 h_F^{-1}\boldsymbol{g}_D, \boldsymbol{w}\rangle_F + \sum_{F\in\mathcal{F}_N(\mathcal{T})} \langle\boldsymbol{g}_N, \boldsymbol{w}\rangle_F \\ &- \sum_{F\in\mathcal{F}_T(\mathcal{T})} \langle(\boldsymbol{g}_T\cdot\boldsymbol{n})\boldsymbol{n}, \boldsymbol{\sigma}(\boldsymbol{w})\boldsymbol{n}\rangle_F + \sum_{F\in\mathcal{F}_T(\mathcal{T})} \beta p_F^2 h_F^{-1} \int_F (\boldsymbol{g}_T\cdot\boldsymbol{n})(\boldsymbol{w}\cdot\boldsymbol{n})\mathrm{d}S. \end{aligned} \tag{24}$$

The first term is the weak implementation of the Dirichlet boundary condition, followed by its stabilising term. The third term is the implementation of the Neumann boundary condition. The fourth is the boundary condition applied on $\partial\mathscr{B}_T$ followed by its stabilising term. For more information on the implementation of problem (20), we invite the reader to refer to Hansbo and Larson.[59]

4 | NUMERICAL CALCULATION OF CONFIGURATIONAL FORCE

Here, we consider the tip[21,22] and domain methods[14] for calculating the CF at the crack tip within the SIPG framework. The tip and domain methods are shown in Figure 2A and 2B, respectively. The tip method considers only the CF value at the crack tip node, marked as white in Figure 2A. The choice of this node is a result of the power dissipated from crack growth being only associated with CF at this node, as discussed in Section 2.3.

The domain method, shown in Figure 2B, considers the CF on the interior set of nodes, marked as white, of elements within the boundary r_d. The motivation for this choice is that the CF values should be zero on the interior set of nodes, except the crack tip node at $\partial\Gamma$. Denzer et al[14] concluded that spurious CF values exist at interior nodes around the crack tip, which should exist at the crack tip. It was found in summing these to the value at the crack tip gave a more accurate solution for the CF. As shown by Irwin,[5] the stresses close to the crack tip are a function of $r^{-1/2}$, where r is a distance from the crack tip. The finite elements within the discretised space struggle to capture the stress singularity, and so the CF, a function of stress, is poorly represented. When using elements, which can capture the stress singularities at the tip,[66] the spurious internal material forces become near zero. When singular elements are used in Scherer et al,[61] a more accurate CF is obtained compared to using conventional finite elements for their examples.

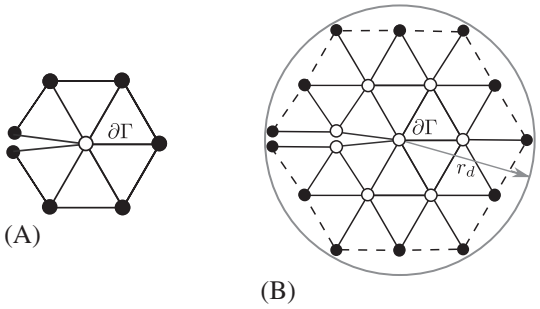

FIGURE 2 The mesh around the crack tip $\partial\Gamma$ showing the nodes, which are considered in the CF calculation using tip A, and domain B, methods

The equation for calculating the CF for the tip and domain method is

$$\boldsymbol{g_I} = -\sum_{n=1}^{n_b}\sum_{K\in A}\int_K \boldsymbol{B_I}^T \Sigma \mathrm{d}V. \tag{25}$$

For the domain, method A is the set of elements K, which have all their nodes within r_d. For the tip method, the set A is the set of all elements K, which have a node on $\partial\Gamma$. Finally, n_b is a list of all nodes in A, which do not lie on the exterior. The white shaded nodes in Figure 2A and 2B are the interior nodes and crack tip node in the set n_b.

Evaluation of (25) is performed in a post-processing procedure after (21) has been solved.

5 | RP-ADAPTIVITY

In this section, we describe a method for propagating a crack in quasi-static rp-adaptive procedure using CF fracture mechanics cast within the presented SIPG finite element framework using hierarchical shape functions.

The benefit to using SIPG is the flexibility available to switch off face interactions between elements by removing the DG face stiffness terms from the global stiffness matrix. This creates new surfaces and is used to propagate a crack. No dof are added to the data structure to propagate a crack whilst only minimal manipulation is required to enable a p-adaptive scheme. The data structure is arranged such that all the dof corresponding to first-order components of all elements are numbered first. The labelling of all these dof is unchanged throughout a simulation, as this is the minimum requirement for a finite element discretisation to exist. All subsequent higher order dof are numbered greater than their first-order counterparts. An example of the data structure is shown in Figure 3.

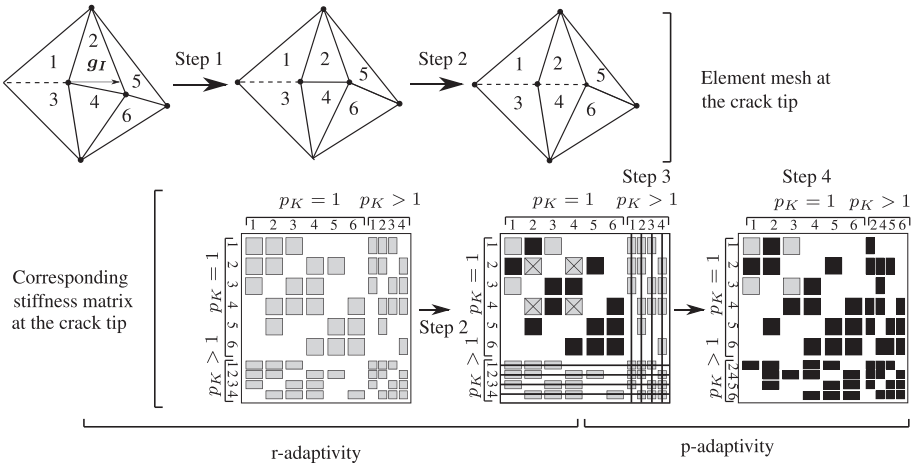

FIGURE 3 rp-Adaptivity for a 6-element mesh at a crack tip, with high-order elements at the tip and the corresponding sparsity matrix. The numbers on the rows and columns of the matrices correspond to element numbers in the mesh

5.1 | Hierarchical shape functions

In this paper, we use shape functions defined for a reference $\hat{K}$ triangular element in Solin et al[64] with improved interior bubble functions. An advantage of the adopted shape functions is that values for an arbitrary high-order shape function can be created in a hierarchical algorithm. This means that it is not necessary to hard code equations for high-order shape functions and an element of an arbitrary high order can be generated.

5.2 | rp-Adaptivity algorithm

In a crack propagation scheme, the CF, $\boldsymbol{g_I}$, is evaluated at each crack tip using either the tip or domain method. If $|\boldsymbol{g_I}| \geq g_c$, then the crack will propagate in the direction $\boldsymbol{g_I}$ and the rp-adaptivity method will be applied as given in Algorithm 1.

An example of a crack propagating through a mesh, using Algorithm 1, with its corresponding changing global stiffness matrix is shown in Figure 3. The mesh is constructed from 6 elements. For the simplicity of this example, only elements sharing a node at the crack tip having a polynomial order, p_K, greater than 1. It is possible to have a group of elements with $p_K > 1$ about the crack tip; these elements reside within the radius r_p. An element is considered inside r_p if at least one of its nodes are inside r_p. To propagate a crack, first, the linear elastic system is solved producing a stress field. $\boldsymbol{g_I}$ is then calculated from the stress field in the material domain, then following Figure 3:

- Step 1, the element face most aligned with $\boldsymbol{g_I}$ is reorientated about the crack tip to be coincident with $\boldsymbol{g_I}$. The face length has size $h_o = \boldsymbol{g_I}/|\boldsymbol{g_I}|\dot{F}_c$, where F_c is the most aligned element face with $\boldsymbol{g_I}/|\boldsymbol{g_I}|$.
- Step 2, the DG face stiffness terms associated with the reorientated face are removed from the global stiffness matrix. This propagates the crack. Their values reside at the positions highlighted by the black "Xs" in the second global stiffness matrix.

Algorithm 1 rp-Adaptivity

Step 1 – r-adaptivity

1: Find nodes within r_d about $\partial\Gamma \rightarrow n_d$.
2: Find interior nodes of the space A, $n_d \rightarrow n_b$.
3: Perform (25) with n_b to obtain $\boldsymbol{g_I}$.
4: Use (17) to get $\boldsymbol{\Delta o_I}$.
5: Create set F, for faces connected to crack node $\partial\Gamma$ with corresponding unit vectors away from crack tip $\boldsymbol{m}$.
6: Identify the most aligned face F_c with $\boldsymbol{\Delta o_I}$ by comparing all $\boldsymbol{m}$ with $\boldsymbol{\Delta o_I}$. Label the most aligned unit vector $\boldsymbol{m}$ as $\boldsymbol{m_c}$, and the corresponding face length L_c:
$F_c = \arg\{\max_{i \in F}(\boldsymbol{\Delta o_I} \cdot \boldsymbol{m}_i)\}$,.[22]
7: Reorientate $\boldsymbol{m_c}$ such that $\boldsymbol{m_c} \times \boldsymbol{\Delta o_I} = \boldsymbol{0}$,.[22] Make the reorientated face length $h_o = \mathrm{g_I}/|\mathrm{g_I}| \cdot L_c$.

Step 2 – Creating a new surface

8: Identify new crack node n_c at the end of face F_c.
9: Remove any further DG face stiffness calculations associated with F_c and delete its values from the global stiffness matrix.
10: Identify all elements with changed vertex coordinates $\rightarrow E_r$.
11: Remove all values in rows and columns, in the global stiffness matrix, for all dof associated with E_r.

Step 3 – p-adaptivity

12: About n_c find nodes within $r_p \rightarrow n_p$.
13: Remove all rows and columns associated with an order $p_K > 1$ for elements not within r_p.
14: Identify elements with $p_k = 1$ which contain nodes n_p and label E_p.

Step 4 – Computation

15: Compute local area and surface stiffness matrices for all dof in set E_r.
16: Compute components of the local area and surface stiffness matrices components associated with a polynomial order > 1 for elements in E_p.
17: Add the newly computed local stiffness matrices components, for $E_r \cup E_p$, to the global stiffness matrix.

This is equivalent to applying homogeneous Neumann boundary conditions on the new crack surfaces. Furthermore, the DG face stiffness matrix calculations for this face are also removed from any further calculations to prevent any face interaction reappearing. This removes any direct interaction between elements along the face creating a new surface, which extends the boundary of the domain, and propagating the crack.

- Step 3, as only elements on the crack tip have a polynomial order greater than 1, and the crack has moved, all rows and columns of the global stiffness matrix associated with the higher order dof of elements no longer at the crack tip are removed.

This is highlighted by the black lines through the final rows and columns of the second stiffness matrix. Additionally, as the geometry of elements, which share a node with the new crack tip, have also changed, all values associated with these elements' local stiffness are removed. This is represented by the solid black blocks in the second matrix.

- Step 4, the updated local stiffness matrix components of elements are added back into the matrix. This corresponds to element with a changed geometry or increase in polynomial order. All new values are highlighted with black boxes in the third matrix in Figure 3.

The specific detail of the rp-adaptive method, which Figure 3 follows, is provided in Algorithm 1. The last stage of Algorithm 1 is recalculating the DG area and surface local stiffness matrices for E_r and E_p and adding them back into the global stiffness matrix. When adding new higher order dof, the only constraint is that their numbering is unique to an element, as with all dof in DG.

5.3 | Average boundary conditions

This type of boundary condition is used for nondeterminant 2D systems. This is the case for linear elastic problems where the displacement is not constrained in both axes. To the author's knowledge that this is the first of its kind implemented for a linear elastic problem. These boundary conditions average the displacements in x and y (u and v), and the rotation, to be 0

$$0 = \int_\Omega u \ \mathrm{d}V \approx \sum_{K\in\Omega} \int_K \boldsymbol{N}_u \boldsymbol{u}_K \mathrm{d}V, \quad 0 = \int_\Omega v \ \mathrm{d}V \approx \sum_{K\in\Omega} \int_K \boldsymbol{N}_v \boldsymbol{v}_K \mathrm{d}V \tag{26}$$

and

$$0 = \int_\Omega \left(\frac{\partial v}{\partial x} - \frac{\partial u}{\partial y} \right) \mathrm{d}V \approx \sum_{K\in\Omega} \int_k \boldsymbol{B}_k \boldsymbol{U}_K \mathrm{d}V. \tag{27}$$

Here, $\boldsymbol{u}_K$ and $\boldsymbol{v}_K$ are dof corresponding to u and v within element K. $\boldsymbol{u}_K = [u_1, 0, u_2 \ \dots \ u_{ndof}, 0]^{\mathrm{T}}$, $\boldsymbol{v}_K = [0, v_1, 0, v_2 \ \dots \ v_{ndof}]^{\mathrm{T}}$, and $\boldsymbol{U}_K = \boldsymbol{u}_K + \boldsymbol{v}_K$, where $_{ndof}$ is the number of dof of a variable within an element. $\boldsymbol{N}_u$ and $\boldsymbol{N}_v$ are arrays of shape functions, $[N_1, 0, N_2, \ \dots \ N_{ndof}, 0]$ and $[0, N_1, 0, N_2, \ \dots \ N_{ndof}]$, respectively,

$$\boldsymbol{B}_K = \left[-\frac{\partial N_1}{\partial y}, \ \frac{\partial N_1}{\partial x}, \ \dots \ -\frac{\partial N_{ndof}}{\partial y}, \ \frac{\partial N_{ndof}}{\partial x} \right]. \tag{28}$$

Equations 26 and 27 are incorporated into the global stiffness matrix and thus form part of the solution.

$$\begin{Bmatrix} \boldsymbol{f_n} \\ \boldsymbol{0} \end{Bmatrix} = \begin{bmatrix} \boldsymbol{K} & \boldsymbol{K_{BC}}^{\mathrm{T}} \\ \boldsymbol{K_{BC}} & \boldsymbol{0} \end{bmatrix} \begin{Bmatrix} \boldsymbol{U} \\ \boldsymbol{\alpha_{BC}} \end{Bmatrix}, \quad \boldsymbol{K_{BC}} = \begin{bmatrix} \int_{k_1} \boldsymbol{N}_u \mathrm{d}V & \dots & \int_{k_{ne}} \boldsymbol{N}_u \mathrm{d}V \\ \int_{k_1} \boldsymbol{N}_v \mathrm{d}V & \dots & \int_{k_{ne}} \boldsymbol{N}_v \mathrm{d}V \\ \int_{k_1} \boldsymbol{B}_1 \mathrm{d}V & \dots & \int_{k_{ne}} \boldsymbol{B}_{ne} \mathrm{d}V \end{bmatrix}, \tag{29}$$

where $_{ne}$ is the number of elements, $\boldsymbol{f_n}$ is $\boldsymbol{l}(\boldsymbol{w})$ evaluated at each node, $\boldsymbol{U}$ contains all displacement dof and $\boldsymbol{\alpha_{BC}}$ is a set of arbitrary unknowns that form part of the solution vector.

6 | NUMERICAL EXAMPLES

In this section, several crack propagation problems are investigated to demonstrate the accuracy of the SIPG for predicting crack paths against analytical numerical benchmark tests and experimental results. All problems considered in this section assume linear elastic material behaviour. Only small strains in plane strain are present with the free energy

function

$$\hat{\psi} = \frac{1}{2}\boldsymbol{\epsilon}^{\mathrm{T}}(\boldsymbol{C}\boldsymbol{\epsilon}), \tag{30}$$

where $\boldsymbol{\epsilon}$ is strain and $\boldsymbol{C}$ is the fourth-order stiffness matrix for linear isotropic elasticity. The accuracy of the numerical scheme for predicting a crack propagation path can be evaluated by considering the CF value and direction for mode 1, mode 2, and mixed mode problems.

6.1 | Single edge notched static tensile test

This static single edge notched (SEN) test is used to show that SIPG method produces CF values within the range of accuracy obtained in literature.[14,21] The value of the CF is dependent on

- the characteristic mesh size at the crack tip h_{cF};
- the domain around the crack tip where elements have $p_K > 1$ defined by the radius r_p; and
- the radius containing all elements used in the domain evaluation of the CF r_d, (25).

Additionally, r_h defines the region around the crack tip where elements are of a different length scale to the rest of the mesh. These variables are also shown graphically in Figure 4A.

The geometry of the test is taken from the benchmark provided by Fagerström and Larsson[19] and is shown in Figure 4A. Here, the crack length $a = 0.1$ m, the width of the plate $b = 0.5$ m, the half height of the plate $H = 1.0$ m, and the uniaxial tensile stress applied is $\sigma = 10$ MPa. The plate has a Poisson's ratio of $\nu = 0.3$ and a shear modulus $\mu = 80$ GPa. Zero average displacement and rotations boundary conditions were applied using (26) and (27). Last, the mesh was generated using the unstructured mesh triangle generator, Triangle,[67] and is shown in Figure 4B. All h-refinement occurred in a homogeneous manner uniformly across the entire mesh, as in Figure 5.

An analytical solution of the energy release rate for the plane stress problem, in Figure 4A, for the mode 1 crack path is derived from the J-integral,

$$G = J = \frac{K_I^2(1-\nu)}{2\mu}, \tag{31}$$

where the empirically corrected SIF, K_I, can be determined from multiple empirical equations provided by Tada et al.[68] So not to be biased, we choose to define a range in the SIF and therefore also the expected energy release rate. The range is provided by the empirical equations, which give the smallest and largest K_I values in Tada et al,[68] respectively:

$$\frac{K_I}{K_o} = 0.265\left(1-\frac{a}{b}\right)^4 + \frac{0.857 + 0.265\frac{a}{b}}{(1-\frac{a}{b})^{\frac{3}{2}}}, \tag{32}$$

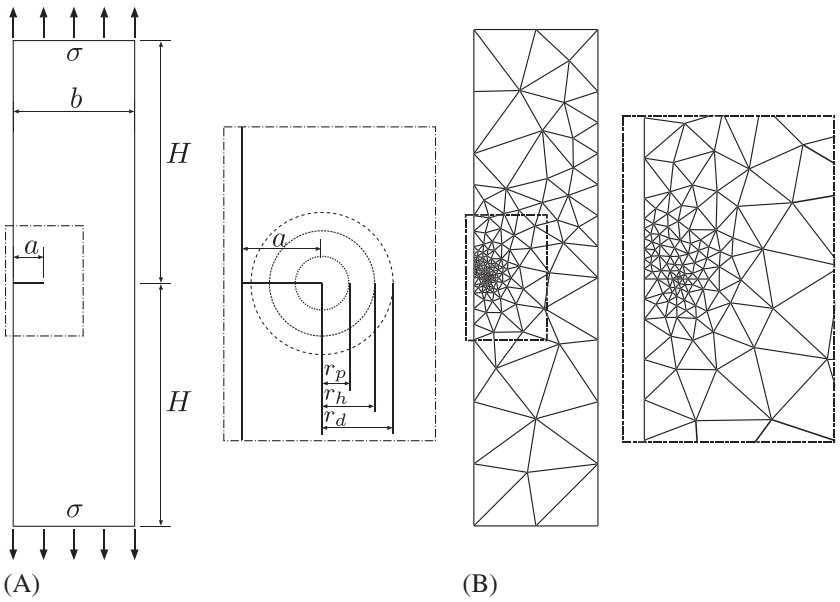

FIGURE 4 Single edge notched (SEN) example: A, Geometry and loading conditions of SEN specimen. B, Mesh of SEN specimen

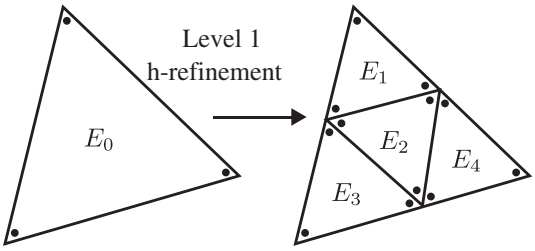

FIGURE 5 A level 1 homogeneous mesh refinement of triangular element E_0 into 4 new elements. The nodes of the new elements either lie on the middle of the edges, or nodes, of E_0

TABLE 1 Comparison of error results for calculating the CF at the crack tip for the static SEN problem against methods using a CG framework

Author	Type of CF evaluation	Element type (Order at around tip)	Minimum error (CF magnitude)
Miehe et al[21,22]	Tip	1st	$2-16\%$
Miehe et al[21,22]	Domain	1st	$2-8\%$
Bird et al	Tip	1st	2.9%
Bird et al	Domain	1st	2.1%
Bird et al	Domain	3rd	1.6%

and

$$\frac{K_I}{K_o} = \sqrt{\frac{2b}{\pi a}\tan\frac{\pi a}{2b}} \cdot \frac{0.752 + 0.202\frac{a}{b} + 0.37(1-\sin\frac{\pi a}{2b})^3}{\cos\frac{\pi a}{2b}}. \tag{33}$$

Using the SIF, $K_o = \sigma\sqrt{\pi a}$ for an infinite plate with a crack length of $2a$.[5] The energy release rate for the mode 1 SEN problem is in the range $G \in [256.7, 261.8]$ N/m. As the finite element solutions converge from below for h and p refinements, we will consider $G = 261.8$ N/m as our reference solution and comment all percentage differences from this value, unless stated otherwise. Considering virtual work in the direction of mode crack propagation, the reference mode 1 CF value is $g = 261.8$ N.

6.2 | SEN static tensile test results

The first investigation was conducted to verify that using SIPG, it was possible to obtain accuracies within the range obtained in literature for CF using CG methods, see Table 1. Given that the most accurate results obtained in both Denzer et al and Miehe et al[14,21] were obtained using the domain method, this method was used to compute the CF for the problem described in Figure 4A, Section 6.1.

First, we investigated how varying r_d around the crack tip affected the accuracy of the CF. For this test, $r_h = 0.1$ m and $p_K = 1$ for all elements. The initial element length within r_h was set to 0.04 m and graded to 0.34 m outside r_h. The mesh refinement was uniform, as in Figure 5.

The changes in CF magnitude when considering element rings to compute the domain evaluation of the CF (25), Figure 6 is consistent with Denzer et al and other works.[14,69-72] We demonstrate that the CF domain integral[14] is poorly represented by all refinement levels when only considering elements at the tip (ring 0). This is followed by a large increase in accuracy, $\approx 20\%$ for all refinements. After this initial jump, an overall average $\approx 1\%$ increase in accuracy between 1 and 4 rings of elements occurs; however, it is noted that increasing the ring size in this region does not guarantee an improvement, and indeed, even with refinement, an improvement for an element ring size is not guaranteed. For instance, Thoutireddy and Ortiz[60] exploited the fact that the CF is dependent on the mesh for a mesh improvement strategy. If an increase in the element rings includes a section of poor mesh, the domain evaluated CF could be perturbed leading to a worse result.

The lack of CF angle convergence, both when increasing element ring size and refining the mesh for a ring size, is demonstrated in Figure 7A. However, when considering a fixed area, which is dictated by the element ring size on the most coarse mesh, Figure 7B, monotonic convergence is achieved with uniform homogeneous mesh refinement. The domain integral in its continuous form[14] is evaluated by considering an area around the crack tip. In the finite element

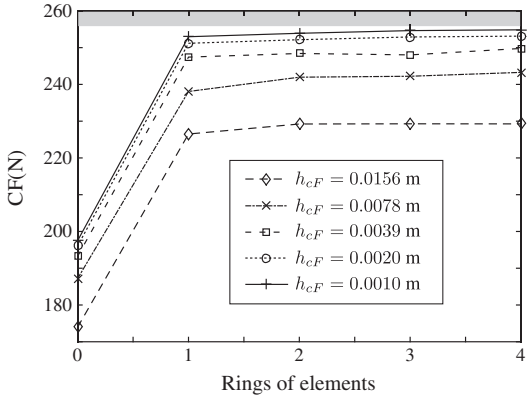

FIGURE 6 Configurational force magnitude, for different mesh refinements at the crack tip, the range in the empirical solution of g is marked in grey

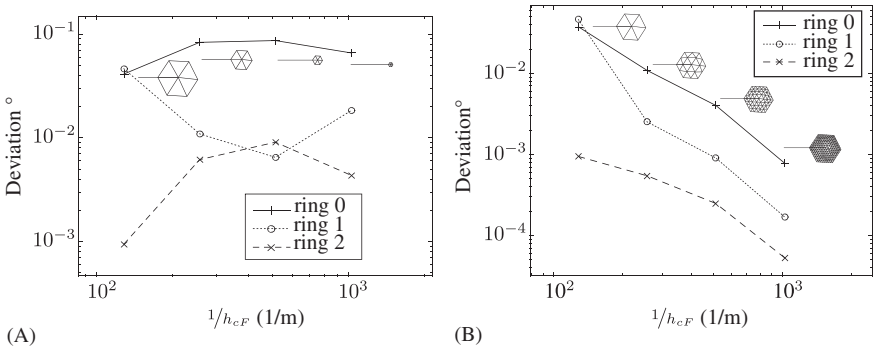

FIGURE 7 SEN: A, How the CF derivation angle changes with element size at the crack tip and when considering different rings of elements around the crack tip when computing (25). B, How CF derivation angle varies when considering the same area of elements, dictated by the element ring area on the coarsest mesh, when computing (25) for different mesh refinements. Example meshes of the elements considered for the computation of the CF are shown for ring 0 in both (A) and (B)

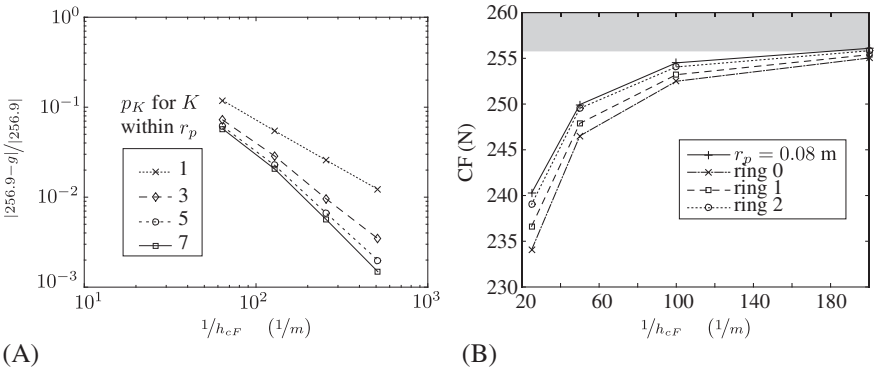

FIGURE 8 SEN: A, varying polynomial order, p_K, of elements within $r_p = 0.05$ m; B, varying the number of $p_K = 5$ elements modelling the stress field around the crack tip for different mesh refinements. The range in the empirical solution of g is marked in grey

formulation if the area for computing the domain evaluated CF is fixed, and uniform homogeneous refinement occurs, the stress solution will improve in this area. Therefore, the domain integral, represented here as the summation of CF nodal values, will improve monotonically.

The next investigation demonstrates how varying element polynomial order around the crack tip affected the accuracy of the CF magnitude with homogeneous mesh refinement. The initial mesh is displayed in Figure 4B.

In Figure 8A, $r_d = 0.08$ m and $r_p = 0.05$ m, both are kept constant. The polynomial order p_K of elements within r_p at the crack tip was varied.

To demonstrate convergence rates for this problem, a value $g = 256.9$ N for the CF was obtained using a structured mesh with greater than 10^6 dof with $h_{cF} = 9.8 \times 10^{-5}$ m. This value is within the range presented in Section 6.1 by the empirical Equations 32 and 33. Figure 8A demonstrates that refinement in either h or p converges to a CF value of $g = 256.9$ N. For all polynomial orders, monotonic convergence was achieved with uniform h-refinement (Figure 5). h-Refinement converges more efficiently than p-refinement as the stress is singular at the crack tip.[5] This agrees with the analytical convergence studies obtained in Pin and Pian[73] and Schwab[74] where it was shown for problems with a singularity h-refinement is more efficient than p-refinement. Overall a minimal error of 1.1% for $p_k = 7$ against the upper bound of g.

Last, in Figure 8B, the rings of elements around the crack tip where $p_K = 5$ is varied whilst r_d remains constant at 0.08 m. It demonstrates that the accuracy of the CF solution is more dependent on the rings of elements around the crack, which have $p_K = 5$ rather than r_p. By having 2 element rings of high-order elements around the tip. The CF error reduces by 7.32% whilst the radius for considering 2 element rings decreases by 8.75 times.

To be consistent, the error values in Table 1 are found using the same empirical solution for this problem found in Miehe et al and Miehe and Gürses[21,22]; here, $g = 259.1$ N. The SIPG obtains results in the range found in literature for CF values.

6.3 | Single edge notched quasi-static crack propagation test

The SEN quasi-static crack propagation test, presented here, has the same geometry as the previous section. Here, weakly imposed heterogeneous Dirichlet boundary conditions are applied for a displacement of 0.01 m at the top and bottom of the specimen. These act in place of the uniaxial tensile stress shown in Figure 4B. The specimen had a Griffith failure criterion $g_c = 1000$ N/m. The mesh is shown in Figure 9C, with an element length graded from 0.04 m around the expected crack path to 0.35 m. For this test, $r_p = 0.08$ m and $r_d = 0.1$ m, the domain of elements with a higher polynomial order moved with the crack tip.

The results for the instantaneous CF deviation from the expected crack direction, of 0°, are shown in Figure 9A and 9B. Each figure shows a total of 8 element face separations. This equates to a total crack path length across the plate of 0.31 and 0.30 m, for Figure 9A and 9B, respectively. The figures demonstrate the improvements gained by using the domain approach. The domain method obtained a maximum difference, from 0°, of 0.09° compared to the tip evaluation, which achieved 0.55°. The figures show how the path direction is governed by integration scheme more than the polynomial order of elements around the tip. The average difference between $p_K = 1$ and $p_K = 7$ for the domain approach was 0.029°, and for the tip approach was 1.86°.

6.4 | Double notched 2-holed quasi-static crack propagation test

This benchmark, taken from Bouchard et al,[34] is a tension test of a double edge notched specimen with 2 holes for mixed mode problems; the geometry and loading conditions are shown in Figure 10A.

This test is necessary to show that SIPG can produce accurate results, compared to CG, for the mixed mode crack propagation problems. The plate acts in plane strain and has a shear modulus $\mu = 8$ GPa, Poisson's ratio $\nu = 0.3$, and a Griffith failure criterion of $g_c = 1000$ N/m. In Figure 10B, the mesh is refined around the crack tips as in Miehe and Gürses[22]; this is to ensure a more valid comparison.

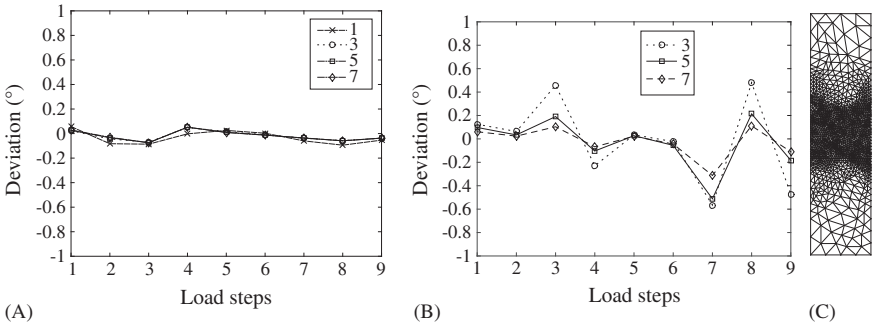

FIGURE 9 Single edge notched crack propagation direction: A, using the domain method,[14] to calculate g_I; B, using the tip method to calculate g_I[22]; and C, the initial mesh used for both (A) and (B)

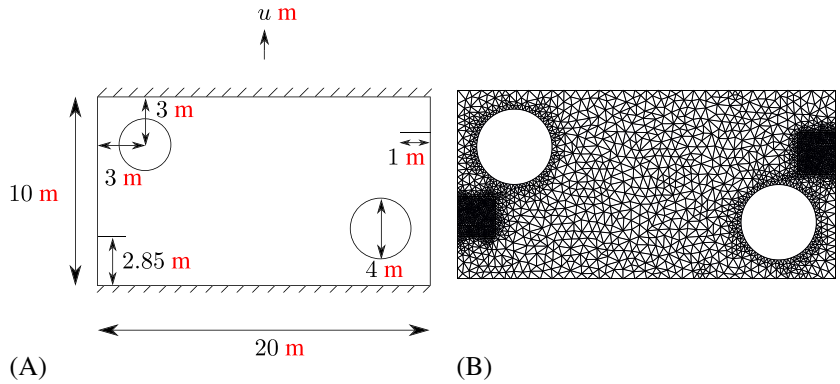

FIGURE 10 Double crack and hole example: A, geometry for the 2-holed quasi-static crack propagation test and B, starting mesh with element length of 0.3 m refined to 0.015 m at the crack tips

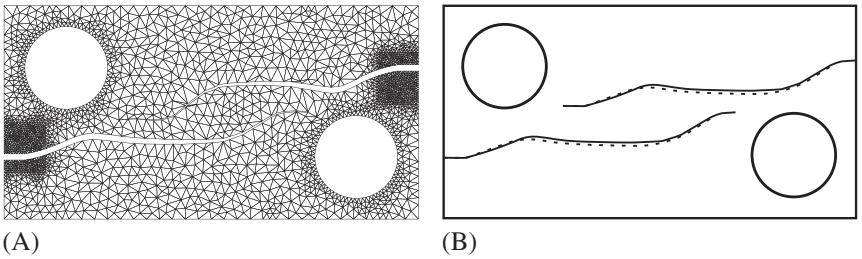

FIGURE 11 Double crack and hole example: A, propagation path and deformed mesh using the domain evaluation method of the CF[61] where the displacements have been magnified by a factor of 10 and B, a comparison of paths between those obtained in Figure 11A (solid line) and the path obtained by Miehe and Gürses[22] (dashed line)

Here, $r_p = 0.1$ m, with elements of polynomial order of 3 within r_p and 1 elsewhere. The CF domain method[14] with $r_d = 0.2$ m was used to evaluate this mixed mode problem. The 2 cracks propagate simultaneously in the same load step. The deformed mesh is shown in Figure 11A. The crack propagation path obtains a good agreement with Miehe et al[22] as shown in Figure 11B.

A slight variant of the experiment, shown in Figure 11A, was performed with the same material properties, loading conditions, radii r_d and r_p, and polynomial order distribution. The experiment analysed the precision of the crack propagation. As the problem is symmetric, the 2 cracks paths in the problem should have the same normalised position relative to their starting point. The difference in the crack paths is a measure of the precision. The results are displayed in Figure 12A; however, it is important to note that the difference in the crack paths is empathise by the x and y axes being different scales.

The precision was measured as the maximum percentage difference from the mean of the 2 crack paths. The coarser mesh, element length of 0.25 m, obtains a precision of 20%. The refined mesh, element length of 0.123 m, achieved a precision of 2%. The lack of precision is caused by 2 features. First, for a coarse unstructured mesh, the stress field is poorly represented. This means on the first load step the configuration force is unlikely to be the same at both crack tips, and so the 2 cracks will propagate in slightly different directions. Secondly, as the increase in crack length $\Delta \boldsymbol{o}$ is larger for the coarse mesh, the error in crack path is magnified. This results in a diverging crack path, Figure 12A, and different stress fields at the tips, Figure 13B. The locations of the new crack tips and the stress fields, Figure 13a, now contrast more than if a finer mesh was used, Figure 12A. Ultimately, the difference between the stress fields and the error in crack path compounds the inaccuracy as the crack propagates through the specimen.

6.5 | Mixed mode single crack propagation in a beam

In this section, a mixed mode single crack propagation problem in a double cantilever beam is analysed; the problem was first described by Belytschko and Black.[75] The problem is described in Figure 14A; it considers a fixed beam with a centre

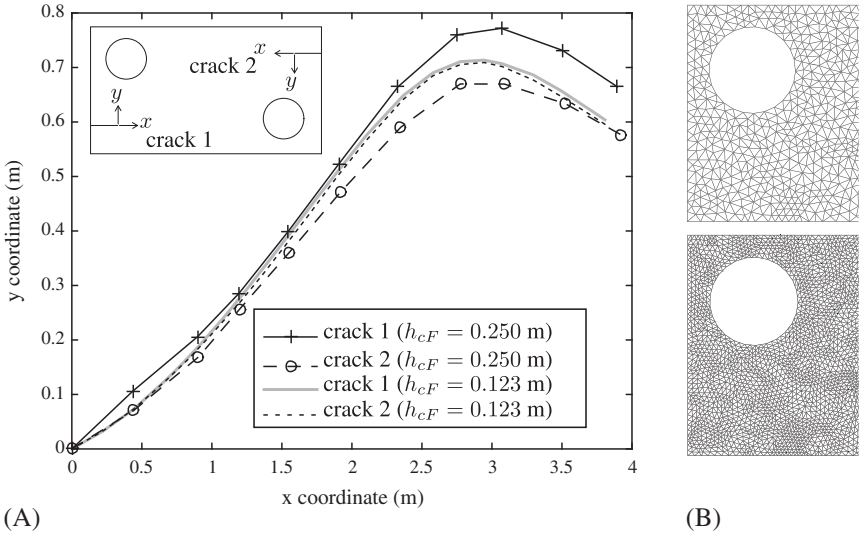

FIGURE 12 Double crack and hole example: A, crack propagation paths for the 2 different mesh refinements in B, where $h_{cF} = 0.250$ m (top right) and $h_{cF} = 0.123$ m (bottom right)

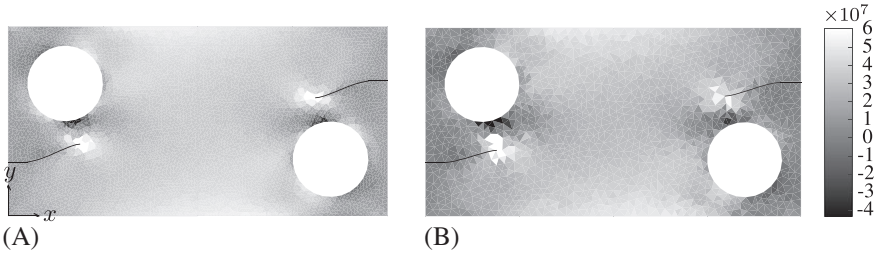

FIGURE 13 Double crack and hole example: plot of σ_{xx} (Pa) for A, $h_F = 0.123$ m and B, $h_F = 0.250$ m

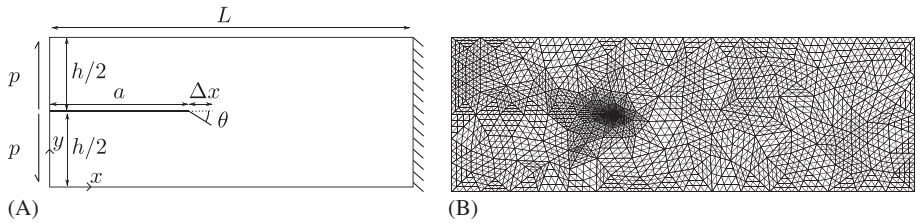

FIGURE 14 Crack in a beam problem schematic A, with the corresponding mesh B

crack where the tip perturbed by a small angle. A traction is applied to the end of beam such that the 2 halves are pulled apart. The problem acts in plane stress, with $L = 0.3$ m, $h = 0.1$ m, $a = 0.1$ m, $p = 0.175$ N/m, $\Delta x = 7.6$ mm, $g_c = 500$ N/m, $\theta = 5.41°$, $E_Y = 206.8$ GPa, and $\nu = 0.3$. The crack is propagated using (17) with, $r_d = 0.01$ m and $p_K = 2\ \forall K \in \mathcal{T}$.

The crack step is dictated by the side length of elements in the mesh; Figure 14B elements are graded from 1/400 m at the crack tip to 1/200 m at the far field. The resultant crack path using (17) with the SIPG face splitting method is compared against the XFEM methods using the MCSC,[75,76] and against the cracking particle method, which also uses MCSC.[77]

The resultant crack paths are displayed in Figure 15. It is important to note that the axes are different scales and the axes are also normalised with respect to the maximum length of the plate in the axes' orientation. Very similar results are obtained between CF SIPG, XFEM MCSC,[76] and the cracking particle method MCSC.[77] The only outlier is Belytschko and Black[75]; however, the general shape of their crack path is similar. In this paper, we choose the CF method,[21] as this method maximises the power dissipation through crack growth, derived from the second law of thermodynamics.

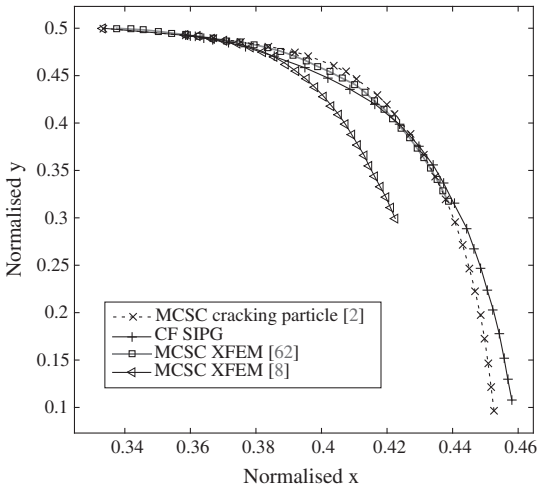

FIGURE 15 Comparison of crack paths, for the crack in a beam problem 14A, using the SIPG CF crack path criterion (17), XFEM MCSC,[75,76] and the MCSC cracking particle method.[77] The axes x and y correspond to the same orientation as in Figure 14A

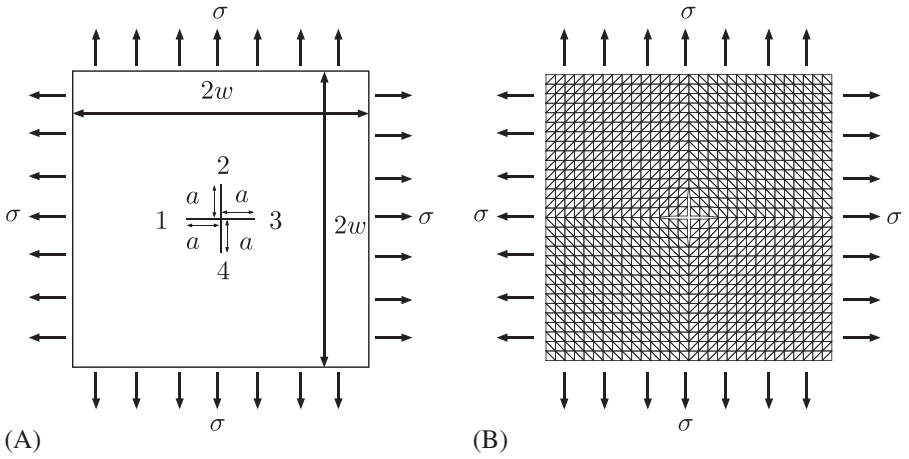

FIGURE 16 Cross crack: A, problem geometry where $2w = 1$ m, the cracks at the centre have a length $a = 0.1$ m with the cracks labelled to 1 to 4. B, the deformed structured symmetric mesh with element face length $h_{cF} = 1/30$ m before propagation, with the displacement scaled by a factor 10^3

6.6 | Quasi-static cross crack propagation in a finite plate

The final numerical example is taken from Sukumar and Belytschko,[78] shown in Figure 16A. The example is used here to investigate the consistency in CF values within a numerical experiment for 2 different boundary conditions, the average boundary conditions presented in Section 5.3 and a fixed bottom left corner node. The plate has a shear modulus $\mu = 8$ GPa, Poisson's ratio $\nu = 0.3$, and a Griffith failure criterion of $g_c = 1000$ N/m. The traction σ acting perpendicular to the plate surface has a value of 10 MPa. The problem is a symmetric plate biaxial loaded, acting in plane strain, with 4 crack tips orientated in a cross.

The cracks are propagated using the r-adaptive method combined with the face splitting algorithm presented in this paper. The increase in crack length for each crack propagation step is the same as the characteristic element size of the mesh, $1/30$ or $1/50$ m and corresponds to splitting of one element face. $p_K = 1$ everywhere, and the tip method was used to investigate the effect the different boundary conditions had on the CF value at the crack tip node. This ensures that only the boundary conditions can cause any disparity in CF values at the crack tips. It is possible for the domain method to capture a different number of elements around the crack tip depending on the element distribution. Each crack was propagated at the same rate. The mesh generated was structured and symmetric; the mesh before crack propagation is shown in Figure 16B.

Each crack should undergo mode 1 propagation; the CF vector should therefore only have one non-zero component, which, in this example, is parallel with the crack lips. The first investigation is designed to isolate the effect the different boundary conditions have on the CF value at each crack tip. Therefore, a symmetric structured mesh is used as in Figure 16B. The magnitude of the deviation of the CF away from its expected direction for each crack tip is represented the by angle between its vector components as shown in Figure 17.

Figure 17 shows that refining from $h_{cF} = 1/30$ m to $h_{cF} = 1/50$ m shows no improvement or even a worse representation of the crack path. The fixed corner makes the problem nonsymmetric by introducing a reaction force. Therefore, the boundary conditions are not sufficient for pure mode 1 crack propagation; hence, it is unachievable, even with refinement. However, the boundary condition does conserve symmetry in one respect as the deviation angle is the same for all cracks, within computational accuracy.

The range of the deviation angle for the 4 cracks using the average boundary conditions is shown Figure 17 by the greyed regions in the graph. The crack path deviation is within the order of computational error for both $h_{cF} = 1/30$ m and $h_{cF} = 1/50$ m. The example demonstrates that the average boundary conditions are suitable to obtain pure mode 1 fracture. The crack path deviation is at least an order 8 times more accurate than that obtained with the fixed corner boundary condition.

Finally, the norm of the CF values at each of the 4 cracks, see Figure 18B, is compared using an unstructured mesh with average boundary conditions and an average $h_F = 1/30$ m, Figure 18A. The cracks undergo 8 element face splits corresponding to a total crack length increase of ≈ 0.27 m. The percentage difference of the CF, from the average value, for each crack ranges from $\pm 0.39\%$ to $\pm 1.24\%$. For the symmetric mesh in Figure 16B, the CF values were found to be the

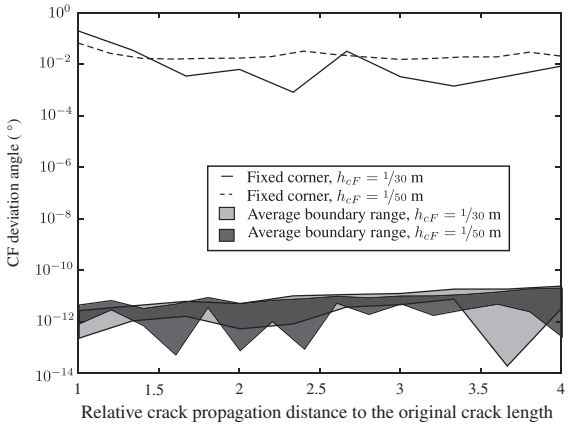

FIGURE 17 The deviation angle of the CF for a structured homogeneous meshes with the same pattern as in Figure 16B for different element face length $h_{cF} = 1/30$ m and $h_{cF} = 1/50$ m. The results for average and fixed corner boundary condition are displayed

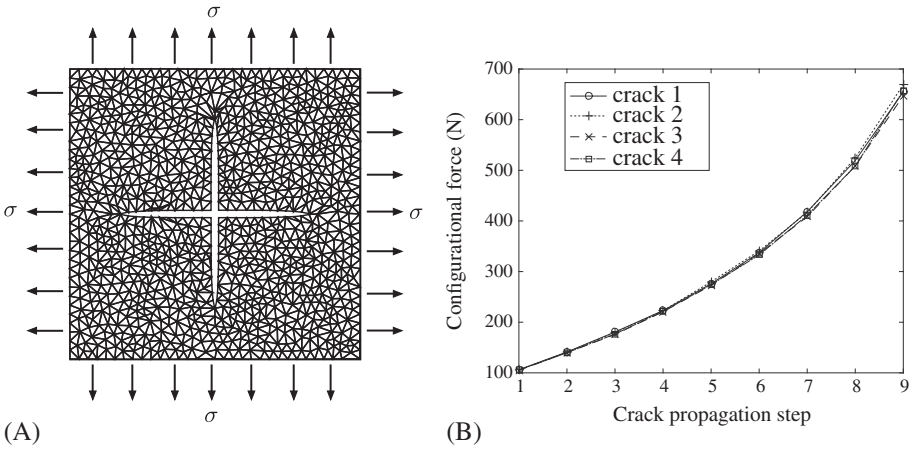

FIGURE 18 A, Resultant unstructured mesh with element length 1/30 m after 9 propagation steps with the displacement scaled by a factor of 10^3. B, Mode 1 CF components for each of the 4 cracks

same for each crack. The range here is therefore generated by the nonsymmetry of the unstructured mesh. At $a = 0.1$ m, the mean CF value is 105.6 N; this is comparable to the XFEM solution calculated in Sukumar and Belytschko[78] where a value of 102.9 N was obtained, via a J-integral domain evaluation.

7 | CONCLUSION

In this paper, we have used the thermodynamically consistent framework presented by Miehe and coworkers[21-23] to model brittle fracture for small strain problems in a SIPG finite element method. The proposed method exploits the element specific dof and the weak interaction between elements and existing as stiffness terms in the global stiffness matrix to propagate a crack in a fashion that is independent of the original element interface orientation. These benefits have not been taken advantage of in the past. In the proposed numerical method, a crack is propagated through (1) moving an element face in line with the CF, (2) removing the DG face stiffness values, in the global stiffness matrix corresponding to the reorientated face, (3) recalculating the local stiffness matrices of elements with changed geometry or polynomial order, and (4) updating the values global stiffness matrix. This r-adaptive procedure in DG adds no dof to the data structure, only the change of local element stiffness values in the global stiffness matrix is required. Additionally we have presented an algorithm to implement arbitrary high-order elements around a moving crack tip and produced an rp-adaptive scheme for SIPG methods. Good agreement for CF values and crack paths was obtained for static and quasi-static, single, and mixed mode problems using the proposed formulation. Mixed mode crack paths using the CF method were also compared against the MCSC method within the numerical framework of XFEM and the cracking particle method. The comparisons were made from results found in literature using existing finite element methods for the same problems. Finally, for non-determinant systems, we introduce an average boundary condition that restrains rigid body motion leading to a solvable system. The proposed average boundary condition method has been shown to achieve machine accuracy for mode 1 crack propagation irrespective of element size for a cross crack problem.

ACKNOWLEDGEMENTS

This work was supported by the Engineering and Physical Sciences Research Council (grant EP/M507854/1). All data created during this research is openly available at https://doi.org/10.15128/r2q237hr92g.

ORCID

Robert Bird http://orcid.org/0000-0002-7070-0462

REFERENCES

1. Eshelby JD. The force on an elastic singularity. *Philos Trans R Soc A*. 1951;224:87-112.
2. Eshelby JD. Energy relations and the energy-momentum tensor in continuum mechanics. *Fundamental Contributions to the Continuum Theory of Evolving Phase Interfaces in Solids: A Collection of Reprints of 14 Seminal Papers*. Berlin, Heidelberg: Springer Berlin Heidelberg; 1999:82-119.
3. Rice JR. A path independent integral and the approximate analysis of strain concentration by notches and cracks. *J Appl Mech*. 1968;35:379-386.
4. Irwin GR. Linear fracture mechanics, fracture transition, and fracture control. *Eng Fract Mech*. 1968;1(2):241-257.
5. Irwin GR. Analysis of stresses and strains near the end of a crack traversing a plate. *SPIE Milestone Series MS*. 1957;137:167-170.
6. Maugin GA. Material force: concepts and applications. *Appl Mech Rev*. 1995;23:213-245.
7. Gurtin ME. *Configurational Forces as Basic Concepts of Continuum Physics*. New York: Springer-Verlag; 2000.
8. Kienzler R, Herrmann G. *Mechanics in Material Space with Applications to Defect and Fracture Mechanics*. New York: Springer-Verlag; 2000.
9. Gurtin ME, Podio-Guidugli P. Configurational forces and the basic laws for crack propagation. *J Mech Phys Solids*. 1996;44:905-927.
10. Steinmann P, Maugin GA, eds. *Mechanics of Material Forces*. New York: Springer-Verlag; 2005.
11. Stumpf H, Le KC. Variational principles of nonlinear fracture mechanics. *Acta Mech*. 1990;83:25-37.
12. Maugin GA, Trimarco C. Pseudomomentum and material forces in nonlinear elaelastic: variational formulations and applications to brittle fracture. *Acta Mech*. 1992;94:1-28.
13. Steinmann P, Ackermann D, Barth FJ. Application of material forces to hyperelastostatic fracture mechanics. ii. Computational setting. *Int J Solids Struct*. 2001;38:5509-5526.

14. Denzer R, Barth FJ, Steinmann P. Studies in elastic fracture mechanics based on the material force method. *Int J Numer Methods Eng*. 2003;58:1817-1835.
15. Mueller R, Kolling S, Gross D. On configurational forces in the context of the finite element method. *Int J Numer Methods Eng*. 2002;53(7):1557-1574.
16. Heintz P, Larsson F, Hansbo P, Runesson K. Adaptive strategies and error control for computing material forces in fracture mechanics. *Int J Numer Methods Eng*. 2004;60(7):1287-1299.
17. Mueller R, Maugin GA. On material forces and finite element discretizations. *Comput Mech*. 2002;29(1):52-60.
18. Larsson R, Fagerström M. A framework for fracture modelling based on the material forces concept with XFEM kinematics. *Int J Numer Methods Eng*. 2005;62(13):1763-1788.
19. Fagerström M, Larsson R. Theory and numerics for finite deformation fracture modelling using strong discontinuities. *Int J Numer Methods Eng*. 2006;66(6):911-948.
20. Shen Y, Lew A. An optimally convergent discontinuous galerkin-based extended finite element method for fracture mechanics. *Int J Numer Methods Eng*. 2010;82(6):716-755.
21. Miehe C, Gürses E, Birkle M. A computational framework of configurational-force-driven brittle fracture based on incremental energy minimization. *Int J Fract*. 2007;145(4):245-259.
22. Miehe C, Gürses E. A robust algorithm for configurational-force-driven brittle crack propagation with R-adaptive mesh alignment. *Int J Numer Methods Eng*. 2007;72(2):127-155.
23. Gürses E, Miehe C. A computational framework of three-dimensional configurational-force-driven brittle crack propagation. *Comput Methods Appl Mech Eng*. 2009;198(15):1413-1428.
24. Kaczmarczyk Ł, Nezhad MM, Pearce C. Three-dimensional brittle fracture: configurational-force-driven crack propagation. *Int J Numer Methods Eng*. 2014;97(7):531-550.
25. Runesson K, Larsson F, Steinmann P. On energetic changes due to configurational motion of standard continua. *Int J Solids Struct*. 2009;46(6):1464-1475.
26. Tillberg J, Larsson F, Runesson K. On the role of material dissipation for the crack-driving force. *Int J Plast*. 2010;26(7):992-1012.
27. Näser B, Kaliske M, Müller R. Material forces for inelastic models at large strains: application to fracture mechanics. *Comput Mech*. 2007;40(6):1005-1013.
28. Näser B, Kaliske M, Dal H, Netzker Ch. Fracture mechanical behaviour of visco-elastic materials: application to the so-called dwell-effect. *ZAMM-J Appl Math Mech/Zeitschrift für Angewandte Mathematik und Mechanik*. 2009;89(8):677-686.
29. Özenç K, Kaliske M, Lin G, Bhashyam G. Evaluation of energy contributions in elasto-plastic fracture: a review of the configurational force approach. *Eng Fract Mech*. 2014;115:137-153.
30. Ishikawa H, Kitagawa H, Okamura H. J-integral of a mixed mode crack and its application. 3rd international conference on Mechanical Behavior and Materials. 1980; Cambridge UK. 447-455.
31. Yan AM, Nguyen-Dang H. Multiple-cracked fatigue crack growth by BEM. *Comput Mech*. 1995;16(5):273-280.
32. Erdogan F, Sih GC. On the crack extension in plates under plane loading and transverse shear. *J Basic Eng*. 1963;85(4):519-525.
33. Destuynder Ph, Djaoua M, Lescure S. Quelques remarques sur la mé,canique de la rupture élastique. *Journal de Mécanique Théorique et Appliquée*. 1983;2(1):113-135.
34. Bouchard PO, Bay F, Chastel Y. Numerical modelling of crack propagation: automatic remeshing and comparison of different criteria. *Comput Methods Appl Mech Eng*. 2003;192(35):3887-3908.
35. Sih GC, Macdonald B. Fracture mechanics applied to engineering problems-strain energy density fracture criterion. *Eng Fract Mech*. 1974;6(2):361-386.
36. deLorenzi HG. On the energy release rate and the J-integral for 3-D crack configurations. *Int J Fract*. 1982;19:183-193.
37. Parks DM. The virtual crack extension method for nonlinear material behavior. *Comput Methods Appl Mech Eng*. 1977;12(3):353-364.
38. Parks DM. A stiffness derivative finite element technique for determination of crack tip stress intensity factors. *Int J Fract*. 1974;10(4):487-502.
39. Parks DM. Virtual crack extension—A general finite element technique for J-integral evaluation. *Numer Methods Fract Mech*. 1978;10:464-478.
40. Hellen TK. On the method of virtual crack extensions. *Int J Numer Methods Eng*. 1975;9(1):187-207.
41. Hellen TK, Blackburn WS. The calculation of stress intensity factors for combined tensile and shear loading. *Int J Fract*. 1975;11(4):605-617.
42. Hansbo A, Hansbo P. An unfitted finite element method, based on Nitsche's method, for elliptic interface problems. *Comput Methods Appl Mech Eng*. 2002;191(47):5537-5552.
43. Hansbo A, Hansbo P. A finite element method for the simulation of strong and weak discontinuities in solid mechanics. *Comput Methods Appl Mech Eng*. 2004;193(33):3523-3540.
44. Heintz P. On the numerical modelling of quasi-static crack growth in linear elastic fracture mechanics. *Int J Numer Methods Eng*. 2006;65(2):174-189.
45. Arranz A, Petrinic N, Süli E. Discontinuous element approximation for dynamic fracture. In: Computational Plasticity Fundamentals and Applications-Proceedings of the 8th International Conference on Computational Plasticity, COMPLAS VIII, number PART 1; 2005; Barcelona. 545-548.
46. Mergheim J, Kuhl E, Steinmann P. A hybrid discontinuous Galerkin/interface method for the computational modelling of failure. *Commun Numer Methods Eng*. 2004;20(7):511-519.

47. Huang H, Costanzo F. On the use of space-time finite elements in the solution of elasto-dynamic fracture problems. *Int J Fract*. 2004;127(2):119-146.
48. Radovitzky R, Seagraves A, Tupek M, Noels L. A scalable 3D fracture and fragmentation algorithm based on a hybrid, discontinuous Galerkin, cohesive element method. *Comput Methods Appl Mech Eng*. 2011;200(1):326-344.
49. Nguyen VP. Discontinuous Galerkin/extrinsic cohesive zone modeling: implementation caveats and applications in computational fracture mechanics. *Eng Fract Mech*. 2014;128:37-68.
50. Wu L, Becker G, Noels L. Elastic damage to crack transition in a coupled non-local implicit discontinuous Galerkin/extrinsic cohesive law framework. *Comput Methods Appl Mech Eng*. 2014;279:379-409.
51. Prechtel M, Ronda PL, Janisch R, et al. Simulation of fracture in heterogeneous elastic materials with cohesive zone models. *Int J Fract*. 2011;168(1):15-29.
52. Abedi R, Hawker MA, Haber RB, Matou K. An adaptive spacetime discontinuous Galerkin method for cohesive models of elastodynamic fracture. *Int J Numer Methods Eng*. 2010;81(10):1207-1241.
53. Tago J, Cruz-Atienza VM, Virieux J, Etienne V, Snchez-sesma FJ. A 3D hp-adaptive discontinuous Galerkin method for modeling earthquake dynamics. *J Geophys Res Solid Earth*. 2012;117(B9).
54. Park K, Paulino GH. Cohesive zone models: a critical review of traction-separation relationships across fracture surfaces. *Appl Mech Rev*. 2011;64(6):060802-060802–20.
55. Reed WH, Hill TR. Triangular mesh methods for the neutron transport equation. Los Alamos Report LA-UR-73-479; 1973.
56. Richter GR. The discontinuous Galerkin method with diffusion. *Math Comput*. 1992;58(198):631-643.
57. Bassi F, Rebay S. A high-order accurate discontinuous finite element method for the numerical solution of the compressible Navier–Stokes equations. *J Comput Phys*. 1997;131(2):267-279.
58. Arnold D. An interior penalty finite element method with discontinuous elements. *SIAM J Numer Anal*. 1982;19(4):742-760.
59. Hansbo P, Larson MG. Energy norm a posteriori error estimates for discontinuous Galerkin approximations of the linear elasticity problem. *Comput Methods Appl Mech Eng*. 2011;200(45):3026-3030.
60. Thoutireddy P, Ortiz M. A variational r-adaption and shape-optimization method for finite-deformation elasticity. *Int J Numer Methods Eng*. 2004;61(1):1-21.
61. Scherer M, Denzer R, Steinmann P. On a solution strategy for energy-based mesh optimization in finite hyperelastostatics. *Comput Methods Appl Mech Eng*. 2008;197(6):609-622.
62. Kuhl E, Askes H, Steinmann P. An ALE formulation based on spatial and material settings of continuum mechanics. Part 1: generic hyperelastic formulation. *Comput Methods Appl Mech Eng*. 2004;193(39):4207-4222.
63. Maugin GA. *Configurational Forces: Thermomechanics, Physics, Mathematics, and Numerics*. Boca Raton: CRC Press; 2016.
64. Solin P, Segeth K, Dolezel I. *Higher-Order Finite Element Methods*. Boca Raton: CRC Press; 2003.
65. Arnold D, Brezzi F, Cockburn B, Marini D. Unified analysis of discontinuous Galerkin methods for elliptic problems. *SIAM J Numer Anal*. 2002;39(5):1749-1779.
66. Barsoum RS. Triangular quarter-point elements as elastic and perfectly-plastic crack tip elements. *Int J Numer Methods Eng*. 1977;11(1):85-98.
67. Jonathan RS. Adaptive precision floating-point arithmetic and fast robust geometric predicates. *Discrete Comput Geom*. 1997;18(3):305-363.
68. Tada H, Paris PC, Irwin GR. *The Stress Analysis of Cracks*. Hellertown PA: Del Research Corp; 1973.
69. Denzer R, Menzel A. Configurational forces for quasi-incompressible large strain electro-viscoelasticity application to fracture mechanics. *Eur J Mech - A/Solids*. 2014;48:3-15. Frontiers in Finite-Deformation Electromechanics.
70. Kuhl E, Denzer R, Barth FJ, Denzer PR. Application of the material force method to thermo-hyperelasticity. *Comput Methods Appl Mech Eng*. 2004;193(3032):3303-3325. Computational Failure Mechanics.
71. Ochensberger W, Kolednik O. A new basis for the application of the J-integral for cyclically loaded cracks in elastic–plastic materials. *Int J Fract*. 2014;189(1):77-101.
72. Menzel A, Denzer R, Steinmann P. Material forces in computational single-slip crystal-plasticity. *Comput Mater Sci*. 2005;32(34):446-454.
73. Pin T, Pian THH. On the convergence of the finite element method for problems with singularity. *Int J solids Struct*. 1973;9(3):313-321.
74. Schwab C. *P-and Hp-Finite Element Methods: Theory and Applications in Solid and Fluid Mechanics*. Oxford: Oxford University Press; 1998.
75. Belytschko T, Black T. Elastic crack growth in finite elements with minimal remeshing. *Int J Numer Methods Eng*. 1999;45(5):601-620.
76. RicMenzel AL, Hegemann J, Sifakis E, Hellrung J, Teran JM. An xfem method for modeling geometrically elaborate crack propagation in brittle materials. *Int J Numer Methods Eng*. 2011;88(10):1042-1065.
77. Ai W, Augarde CE, Int J Numer Methods Eng. An adaptive cracking particle method for 2d crack propagation. 2016;108(13):1626-1648.
78. Sukumar N, Belytschko T. ARbitrary branched and intersecting cracks with the extended finite element method. *Int J Numer Methods Eng*. 2000;48:1741-1760.

How to cite this article: Bird R, Coombs W, Giani S. A quasi-static discontinuous Galerkin configurational force crack propagation method for brittle materials. *Int J Numer Meth Engng*. 2018;113:1061–1080. https://doi.org/10.1002/nme.5699